Optics & Laser Technology 179 (2024) 111351

Contents lists available at ScienceDirect

Optics and Laser Technology

journal homepage: www.elsevier.com/locate/optlastec

Full length article

Monitoring of three-dimensional live-cell cultures using a multimode, multiscale imaging system combining confocal fluorescence microscopy and optical coherence microscopy

Naresh Kumar Ravichandran [a,1], HyeMi Kim [a,1], Joonha Park [b,1], Hwan Hur [a], Jinsung Kim [a], Ji Yong Bae [a], Sangwon Hyun [a], I Jong Kim [a], Dong Uk Kim [a], Sang-Chul Lee [a], Ki Soo Chang [a], Inbarasan Muniraj [c], Jessie S. Jeon [b,*], Ki-Hwan Nam [a,*], Kye-Sung Lee [a,*]

[a] Center for Scientific Instrumentation, Korea Basic Science Institute, 169-148 Gwahak-ro Yuseong-gu, Daejeon 34133, Republic of Korea
[b] Department of Mechanical Engineering, Korea Advanced Institute of Science and Technology, Daejeon 34141, Republic of Korea
[c] LiFE Lab, Department of ECE, Alliance School of Applied Engineering, Alliance University, Bengaluru, Karnataka 562106, India

ARTICLE INFO

Keywords:
Live-cell monitoring
Fluorescence microscopy
Optical coherence microscopy
Extracellular matrix
Tumor spheroid
Vascular organoid

ABSTRACT

Live-cell monitoring involves long-term observation and analysis of living cells in tissue cultures, which develop cells or tissues in an artificial environment and are essential for tissue engineering. Fluorescence microscopy (FM) is widely used as a monitoring tool owing to its powerful ability to visualize protein distribution within cells and tissues, thereby providing information on their functions in biological processes. To reduce the photobleaching effect, which is a major limiting factor in FM, FM is generally combined with other imaging modalities, such as phase contrast and differential interference contrast microscopy, which are nondestructive to fluorochromes, to selectively use fluorescence signals only in specific areas of interest within a sample. However, these methods are restricted to thin samples and cannot produce depth-resolved images. Here, we propose a method to determine three-dimensional (3D) positions in volumetric samples for application in high-resolution 3D fluorescence imaging using a multimode and multiscale imaging system that combines optical coherence microscopy (OCM) and line confocal FM (LC–FM). We also demonstrate the benefits of multimodal imaging in 3D cell culture monitoring. To evaluate the performance of the proposed system and method, we rapidly and accurately located the regions of interest in 3D tissue culture models, such as tumor spheroids and microvascular bed, and instantaneously acquired volumetric high-resolution fluorescence images. We also used an integrated system to monitor tumor spheroids mixed with extracellular matrix (ECM) over five days of the culture process, and the FM–OCM integrated technique successfully imaged the overall 3D structures, such as the distribution and boundaries of the spheroids and ECM as well as stained tumor cells. This complementary information is useful for understanding the relationship between cellular behaviors, such as the proliferation and migration of tumor cells, and microenvironments, such as the ECM.

1. Introduction

Live-cell monitoring, the process of observing and recording the behavior of living cells over time, is used to examine cellular behavior and interactions in real time and can provide valuable insights into the mechanisms underlying the cellular processes [1–3]. Cell biologists primarily use fluorescence microscopy (FM) because it allows real-time visualization of specific cellular processes [1,3]. Fluorescent labeling can be used to stain specific proteins or organelles within cells, allowing the visualization of their behavior and interactions over time, such as cellular migration and interactions [4,5], vascular growth [6], and neuronal activity [7]. However, FM has several limitations in live-cell

Abbreviations: FM, fluorescence microscopy; OCM, optical coherence microscopy; ECM, extracellular matrix; ROI, region of interest); FOV, field-of-view; SNR, signal-to-noise ratio.

* Corresponding authors.
E-mail addresses: jsjeon@kaist.ac.kr (J.S. Jeon), namkihwan@kbsi.re.kr (K.-H. Nam), kslee24@kbsi.re.kr (K.-S. Lee).

[1] These three authors contribute to the study equally.

https://doi.org/10.1016/j.optlastec.2024.111351
Received 26 October 2023; Received in revised form 17 May 2024; Accepted 18 June 2024
Available online 30 June 2024

monitoring. One of the main limitations of this method is its phototoxicity, which can lead to cell damage and death over time [8]. Another limitation is photobleaching, which can cause the fluorescent signal to fade over time when fluorescent dyes are subjected to prolonged or repeated imaging [9]. Finally, FM is limited by the number of fluorescent probes that can be used simultaneously, limiting the amount of information that can be obtained from a single experiment [10,11]. To reduce the effects of phototoxicity and photobleaching in FM, fluorescence signals are selectively used in a specific region of interest (ROI) within a sample, typically in combination with other imaging modalities that are nondestructive to fluorochromes, such as phase-contrast and differential interference contrast microscopy [12,13]. In addition, combining these two imaging techniques can provide more complete information about cells and their behavior [12,13]. For example, incorporating a reliable structural confirmation method, such as phase-contrast imaging, prevents misrecognition of cell shapes and boundaries owing to photobleaching, which can occur when only fluorescence-imaging-assisted monitoring is performed [14]. Such methods are necessary for deriving more informed interpretations and draw more accurate conclusions.

Three-dimensional (3D) cell culture involves the growth of cells and tissues in a 3D artificial environment. This allows the study of cell behavior and interactions in a more complex environment that better mimics the *in vivo* environment than traditional 2D cell cultures [15–17]. It also provides a more accurate representation of the extracellular matrix (ECM) and cell–cell interactions [15,17]. Organoids and spheroids are typical products of 3D structures. Organoids are derived from stem cells and can be used to model the organ structure and function in vitro [18], whereas spheroids are formed by the aggregation of cells in a suspension [19]. Numerous studies have been conducted using organoids and spheroids to develop new treatments for diseases and test the safety and efficacy of new drugs before testing them in humans [18]. Owing to the variable and dynamic nature of organoid growth, continuous monitoring of the changes that occur within a sample is necessary [20]. Different types of FM techniques with optical sectioning abilities have been developed for volumetric imaging of 3D tissue models; these techniques include confocal FM [21], line-confocal FM [22], spinning-disk confocal FM [23], two-photon FM [24], optical sectioning wide-field FM [25], and light-sheet FM [26], which have been widely used in live-cell imaging and other monitoring experiments [27]. However, the adverse effects of the aforementioned limitations of FM amplify with the use of 3D FM. Phototoxicity and photobleaching effects may occur more easily owing to long light exposure times during depth scanning for volumetric imaging, and the light emission efficiency decreases when a pinhole aperture is used for optical sectioning. In addition, 2D optical imaging techniques such as phase-contrast microscopy, which are limited to thin samples, cannot grasp the complex structure of a 3D sample tissue.

Optical coherence microscopy (OCM) is a low-coherence interferometry-based imaging technique used to extract volumetric information of biological samples [20,28,29]. Notably, OCM provides intricate high-resolution depth-resolved insights into tissue morphology and microstructure without requiring fluorescence labeling [28,29]. OCM facilitates 3D visualization of tissue architectures, cellular organization, and the spatial relationships between different tissue components [29]. Conversely, FM can effectively reveal the distribution and localization of different types of molecules within tissues. Furthermore, FM is highly sensitive to fluorescent probes and can detect specific molecules within tissue [30]. These features enable labeling of cells or structures of interest using fluorescent markers and allow real-time tracking of their distributions and localization, which are valuable for studying dynamic processes, such as cellular migration and interactions [31] and vascular growth [32]. The integration of OCM and FM enables the visualization of both the structural and functional aspects of the specimen while also facilitating the monitoring of cells labeled with fluorescent markers within the tissue; that is, OCM and FM-integrated multimodal imaging systems leverage the detailed morphological characterization ability of OCM and molecular specificity provided by FM [4,30–36]. However, to date, multimodal imaging systems based on OCM, have been primarily used to obtain complementary information. Here, we propose a multimode and multiscale imaging system that combines OCM and line confocal FM (LC–FM) as well as a method to locate 3D positions in volumetric samples for high-resolution 3D fluorescence imaging. We also demonstrate the benefits of multimodal imaging in 3D cell culture monitoring.

2. Methods

2.1. Multimode and multiscale 3D imaging system combining confocal FM and OCM

Fig. 1 (A) shows the schematic diagram, and Fig. 1 (B) and (C) show the actual photographs of the overall layout of the built OCM-integrated LC–FM multimodal imaging system, which is equipped with two distinct light sources: one for OCM imaging and the other for LC–FM imaging. The OCM uses a superluminescent broadband light source (SLD-37-HP3, Superlum Diodes Ltd., Carrigtwohill, Ireland) with a central wavelength of 840 nm and a bandwidth of 80 nm, which yields an axial resolution of ~ 5 μm. This is shown in the measured OCM graphs in Fig. 1 (H) and (I). In Fig. 1 (H) shows the axial scan plot of a OCM cross-sectional image of a high-reflective surface as a sample, and Fig. 1 (I) is the zoomed-in axial plot of (H) showing the FWHM of intensity peak of ~ 5 μm. The output of the light source was linked directly to the input port of a 50:50 optical fiber coupler (850-H7-L-15-FA, OF-LINK Communications Co., Ltd. Shenzhen, China), which splits the beams into reference and sample arms. Both ends of the optical coupler output port are connected to a doublet collimator (F240APC-850, Thorlabs, Inc., NJ, USA). In the reference arm, the beam travels through a combination of optical components including a continuous variable attenuator (NDC-50C-4 M, Thorlabs, Inc., NJ, USA) and a highly reflective broadband mirror (PF10-03-P01P, Thorlabs, Inc., NJ, USA) mounted on a motorized micro-positioning stage (M30×/M, Thorlabs, Inc., NJ, USA). A motorized stage was employed to adjust the optical path length in the reference arm of the OCM interferometer to match that of the sample arm when using different objectives. The appropriate path lengths in the reference arm were determined in advance and applied automatically when switching between objectives. In the sample arm, a dual-axis galvanometer scanning mirror was used to raster-scan the collimated beam in the XY plane (GVSM002-JP, Thorlabs, Inc., NJ, USA). The scanning beam was directed towards the scan and tube lenses with focal lengths of 54 mm (LSM04-BB, Thorlabs, Inc., NJ, USA) and 200 mm (TTL200-B, Thorlabs, Inc., NJ, USA), respectively. The scanning beam following the tube lens was directed towards the back end of an Olympus IX83 inverted microscope body, where a rotational selection slider was mounted with a dichroic mirror (Di03-R488-t1-25 × 36, Semrock OPTICAL FILTERS, IDEX Health & Science, LLC, NY, USA) for FM imaging and a highly reflective mirror for OCM imaging.

The back-reflected beams from the sample were collected via the objective lens and redirected back to the optical coupler, where the back-reflected light from the sample and reference arms were combined. The combined light was directed to a spectrometer using a 4096-pixel line-scan camera (Sprint spl4096-140 k, Basler AG, Ahrensburg, Germany). The spectrum in the range of 800–880 nm was registered to 2048 pixels of the CMOS line camera employed in the spectrometer and then digitized on a frame grabber. The total maximum imaging depth range attainable with the said camera configuration is 3.27 mm. Real-time visualization of cross-sectional and *en face* OCM images was achieved through signal processing of the acquired signals, such as numerical dispersion compensation, domain conversion, and fast Fourier transform, using a GPU (NVIDIA Tesla K20, NVIDIA Corporation, Santa Clara, CA, USA). The material and number of lenses used differed for each type of objective lens, which induced different dispersions in the sample arm.

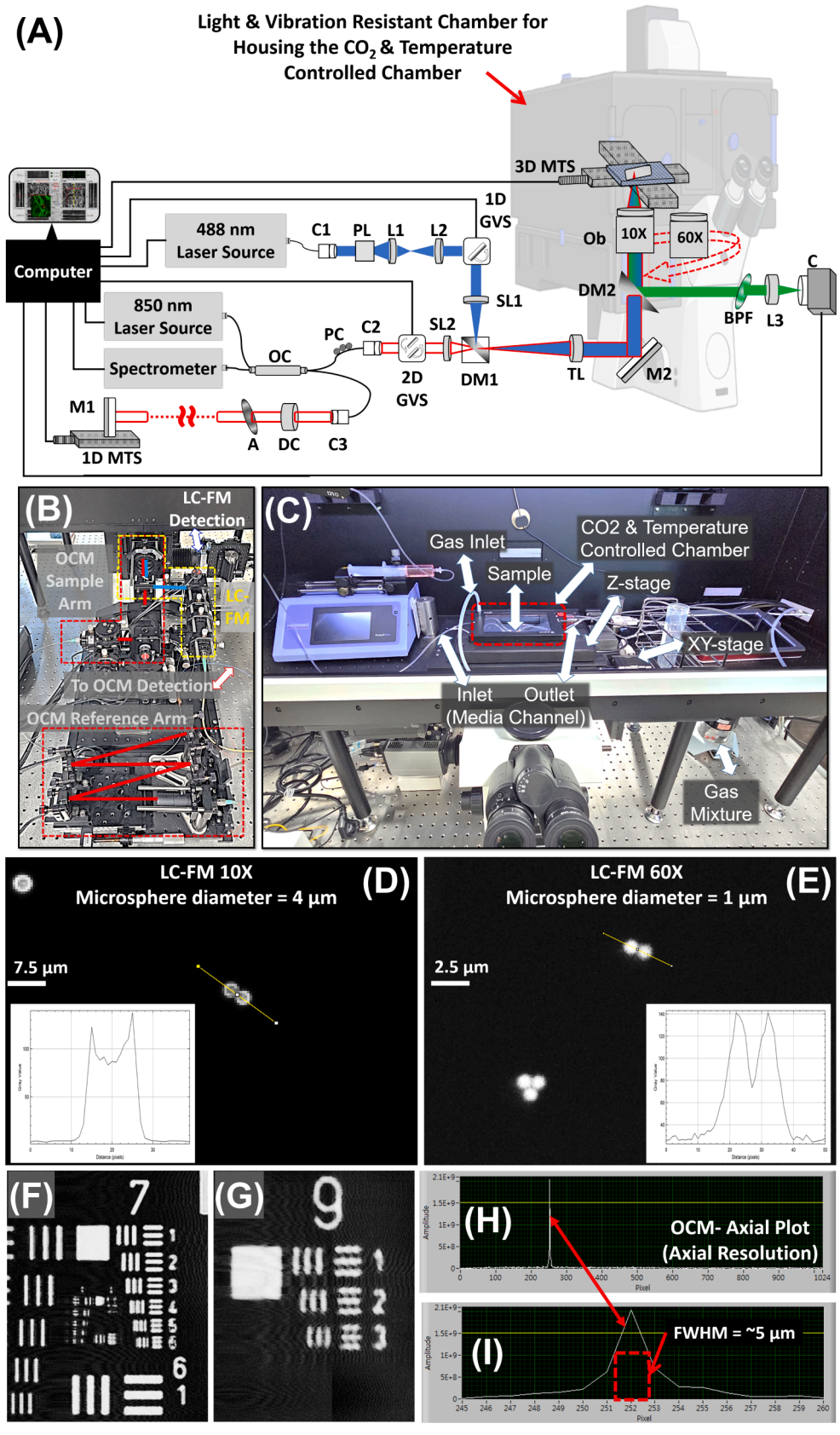

(caption on next page)

Fig. 1. Overall schematic and key performances measured for the integrated multimodal OCM–LC–FM imaging system. (A) is the overall schematic depiction illustrating the multimodal OCM-LC-FM imaging system. (B) and (C) are the actual photographs of the optical setup, and CO_2 and temperature controlled chamber for sample, respectively. (D) is the 10 × LC-FM image of fluorescent microspheres of diameter 4 μm with inset graph showing the profile plotted along the yellow line in (D). (E) is the 60 × LC-FM image of fluorescent microspheres of diameter 1 μm with inset graph showing the profile plotted along the yellow line in (E). (F) and (G) are the *en face* OCM images of USAF 1951 obtained with 10× and 60×, respectively. (H) is the axial plot of an OCM cross-sectional image of a high-reflective surface. (I) is the zoomed-in axial plot of (H) showing the FWHM of ~ 5 μm. The red lines represent the OCM laser beam; the solid blue represents the LC–FM illumination beam; and the solid green represents the LC–FM detection beam. 1D GVS: one-dimensional galvanometer scanning mirror, 1D MTS: one-directional motorized translational stage, 2D GVS: two-dimensional galvanometer scanning mirrors, 3D MTS: three-axes motorized sample translational stage, A: attenuator, BPF: bandpass filter, C: area camera used for LC–FM imaging, C1 to C3: Collimator, DC: dispersion compensator, DM1 and DM2: dichroic mirror, L1 to L3 lenses, M1 and M2: high-reflective silver mirrors, Ob: objective lens, OC: optical coupler, PL: Powell lens, SL1, and SL2: scan lens, TL: infinity-corrected tube lens. Components are not drawn to scale. (For interpretation of the references to colour in this figure legend, the reader is referred to the web version of this article.)

To implement multiscale OCM imaging, it is necessary to preconfigure, select, and apply an appropriate numerical dispersion compensation for each objective lens, such as the optical path length matching mentioned above. The lateral resolution for the built OCM system was calibrated using a USAF 1951 high-resolution target (3″ x 3″ Positive, USAF 1951 Hi-Resolution Target, Edmund optics, Inc., NJ, USA), as shown in Fig. 1 (F) and (G). When used with a 10 × objective (UPlanFL N 10×, numerical aperture (NA) 0.3, Olympus Inc., USA) for low magnification, the maximum element of the resolution target that could be clearly identified in group 7 was element 5 (Fig. 1 (F)), which has 203 line pairs per millimeter which can be translated to a lateral resolution is ~ 5 μm and a maximum field-of-view (FOV) of 1.5 × 1 mm (vertical × horizontal) could be attained. When used with higher magnification of 60 × configuration (UPlanFL N 60×, NA 0.9, Olympus Inc., USA), the maximum element of the target that could be clearly identified in group 9 was element 3 (Fig. 1 (G)), which has 645 line pairs per millimeter which can be translated to a lateral resolution of ~ 1.6 μm with a maximum attainable FOV of 185 × 115 μm (vertical × horizontal). The maximum imaging depth, which is the depth of focus, was calibrated by using a highly reflective surface as a sample, which was translated along the depth axis in both forward and reverse directions from the point of maximum achievable focus using a z-axis nano-positioning stage (ZL500, Mad City Labs Inc.) until the image became defocused. The measured total travel distance when used with 10 × and 60 × were ~ 100 μm and ~ 16 μm, respectively. To obtain a cross-sectional image, a series of 500 lateral locations (A-line) were consecutively scanned to produce one 2D cross-sectional OCM image at a speed of 100 frames per second, and 500 images were acquired consecutively scanned horizontally to generate a volumetric image in 5 s.

We built a custom line-scanning confocal FM system using a CMOS rolling shutter for high-speed 3D FM imaging. The FM imaging system used a laser source (S4FC488; Thorlabs, Inc., NJ, USA) with a central wavelength of 488 nm. The laser beam was collimated using a F220APC-532 collimator (Thorlabs, Inc., NJ, USA) and directed onto a Powell lens (43–473, Edmund optics, Inc., NJ, USA) at a fan angle of 30°, resulting in a uniform laser line by fanning the collimated beam out in one dimension. The fanning-out laser line was then directed toward a combination of two achromatic lenses (TRH127-020-A-ML and TRH254-040-A-ML, Thorlabs, Inc., NJ, USA) to relay on the surface of a 1D galvanometer scanning mirror (GVS001, Thorlabs, Inc., NJ, USA), which was used to scan the line-focused beam generated after passing through a scan lens (LSM03-VIS, Thorlabs, Inc., NJ, USA). A line-focused beam was coupled into the OCM optical path with a dichroic mirror and then formed at the sample plane with the same tube and objective lenses, which were also used for OCM imaging. The fluorescence signal emitted from the sample, which was collected by the objective lens, was guided into the detection path with another dichroic mirror mounted on a rotational selection slider, passed through a bandpass filter (FF03-525/50–25, Semrock LLC, NY, USA), and focused onto the image plane of an sCMOS camera (Zyla 4.2 sCMOS, Andor Technology) using a focusing lens (AC254-300-A, Thorlabs, Inc., NJ, USA). Confocal images were obtained by synchronizing the line field scanning over the sample and the rolling shutter action of the sCMOS camera to remove out-of-focus light. To construct a 3D volumetric image of FM, a z-axis nano-positioning stage (ZL500, Mad City Labs Inc.) with a total travel range of 500 μm was utilized to move the sample along the depth axis. Translational movements along the X-Y axes were achieved using a micropositioning stage (MCL-MOTNZ, Mad City Labs Inc.). The lateral resolution of the LC-FM system was calibrated using a commercially available fluorescence microscope test slide containing variable-size fluorescent microsphere targets (F36909, FocalCheck™ Fluorescence Microscope Test Slide #1, ThermoFishers Scientific, USA). The obtained LC-FM images of the fluorescent microspheres in row A, columns 3 and 4 of the test slide are shown in Fig. 1 (D) and (E), respectively. The LC-FM images shown in Fig. 1 (D) and (E) are obtained using 10 × and 60 × objectives, which shows the fluorescent microspheres of diameters 4 μm and 1 μm, respectively. The inset graphs within Fig. 1 (D) and (E) are the profile plots obtained at the marked yellow lines, which were measured across two adjacent microspheres. In both the inset pots, two distinct peaks can be seen, which correspond to the center of microspheres, which yields that the lateral resolution of LC-FM when used with 10 × and 60 × are better than 4 μm and 1 μm, respectively. Our built LC-FM system offers a maximum of 500 μm travel distance using Z-stage, but when coupled with a 60 × objective lens, the maximum imaging depth from the sample surface is limited to 200 μm, which is the working distance of the objective lens. The maximum FOV attained with current scanning setup were 1000 × 650 μm and 185 × 115 μm for the 10 × and 60 × objective lenses, respectively. The laser line's scanning speed is 20 Hz, which corresponds the acquisition time of 0.05 s for a LC-FM image. To obtain a volumetric LC-FM image, the sample was translated over 100 positions along the depth axis using the z-axis nano-positioning stage. The total time taken to acquire one volumetric LC-FM image was 5 s. For live-cell imaging, the samples were mounted on a sample holder with temperature-controlled gas mixture flow at 37 °C, a live-cell culture system on top of the stage (Incubator System T, LCI, Inc.). The OCM system utilized a Superlum Diodes SLD-37-HP3 as the light source, emitting wavelengths in the range of 800 to 880 nm, with a laser power output of 18 mW. Considering the fact that only 50 % of this is directed towards the sample using the optical coupler and the losses from alignment optics, the effective laser power reaching the sample was approximately ~ 5 mW. For the LC-FM illumination, the laser source S4FC488 was employed, emitting light at 488 nm, with a typical laser power of 2.5 mW (unless mentioned otherwise) for line illumination on the sample. For both OCM and LC-FM, the total time required to obtain one volumetric image is around 5 s. These illumination levels were carefully controlled and maintained, which are well within the established ANSI (American National Standards Institute) safety limits for biomedical samples [37].

2.2. Algorithm to select an ROI in a 3D biochip sample and aim light directly at that ROI using OCM for high-resolution confocal fluorescence imaging

The steps for high-resolution 3D fluorescence imaging at the desired location are shown in Fig. 2. The FOV used to search for ROI was determined by the maximum attainable FOV of the OCM system using the selected objective lens. In this study, a 10 × objective lens was used for the low-magnification OCM imaging, which yielded an FOV of 1.5 × 1.0 × 0.1 mm (X-Y-Z), to search for the ROI within the volumetric

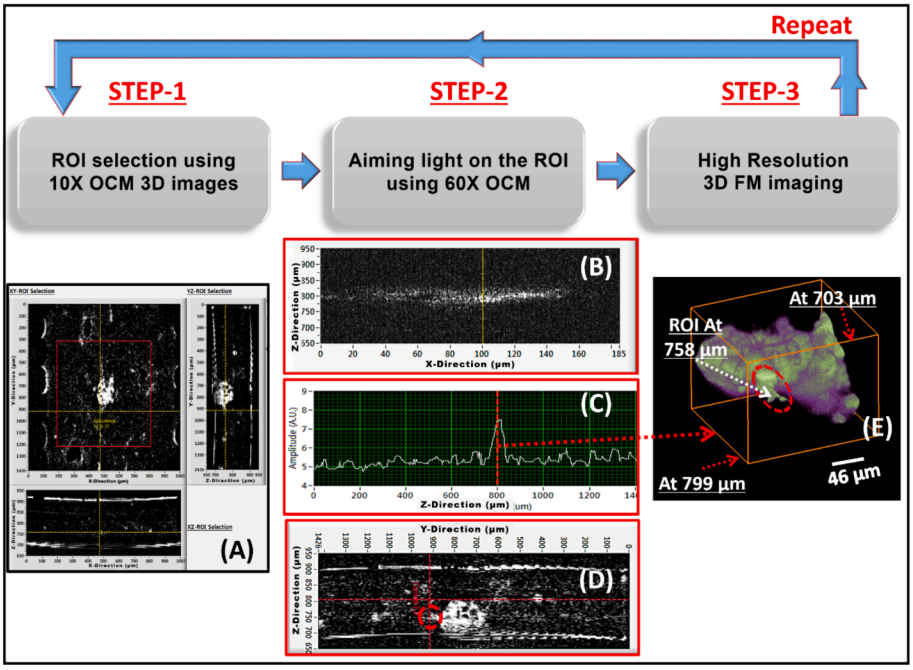

Fig. 2. Steps for high-resolution 3D fluorescence imaging directly at the desired location in a 3D biochip sample. This figure shows the complete method for utilizing OCM to screen biochip samples with complex microenvironments for selecting an ROI, focus light on the ROI, and perform depth boundary calculations for volumetric LC–FM imaging of the selected ROI. (A) is the OCM screening window used for ROI selection. (B)–(D) Focus position visualization onto the ROI and depth limit estimation of ROI for LC–FM volume imaging. (E) is the volumetric LC–FM image of ROI.

sample. The depth of focus was approximately 100 µm when the 10 × objective was used. The acquired 3D OCM image data were saved and visualized in orthogonal views of XY, XZ, and YZ to carefully search for and determine the ROI for high-resolution FM imaging, as shown in Fig. 2(A). The search can be repeated for the entire volume of the sample by moving the X- and Y-positions of the sample and the height of the objective lens. In the second step, when an ROI was selected, the actual distance required to move the sample translation stage along the X- and Y-axes was calculated, and the stage moved the sample such that the target ROI reached the center of the FOV where the objective was located. After obtaining an X-Z cross-sectional image with a 10 × objective lens, it was changed to a 60 × objective lens for high magnification. In the X-Z view of the OCM captured with a 60 × objective lens, an image that resembles a sharp line is formed owing to the narrow depth of focus, as shown in Fig. 2(B). Specifically, the peak position of the line image in the X-Z view corresponded to the depth position of the focal line in the sample, as shown in Fig. 2(C). The peak position was marked on the pre-stored X-Z image captured by the 10 × objective and placed at the desired depth in real time, as shown in Fig. 2(D). If an extended depth of focus over the entire depth of the sample is required for pre-stored X-Z images, multiple X-Z images can be acquired at different focus positions along the depth and then merged. Additionally, the first and last depths of the ROI area can be easily determined by moving the objective lens along the Z-axis because the focus position marked in the pre-stored X-Z image is updated in real time. The measured value was used to set the movement range of the sample stage in the z-axis direction to capture a 3D volumetric image of the ROI. In the final step, after focusing the light at the desired depth, high-resolution FM imaging was performed directly, as shown in Fig. 2(E). The process could be repeated rapidly at any given position within the sample volume in the three axes.

2.3. Sample preparation

The overall architecture of the bio-chip and the environment controlled multimodal imaging system employed for experimental purposes is shown in Fig. 3(A). A brief representation of vascular network formation and the formation of tumor spheroid in bio-chip used for long-term live-cell monitoring experiments is given in Fig. 3(B) and (C), respectively. The microfluidic device vascular-on-chip (VoC) containing a vascular network was constructed using soft lithography, as previously described[38]. Briefly, the microfluidic device was designed to contain three different channels: one gel channel containing the ECM, human umbilical vein endothelial cells (HUVECs) transduced with green fluorescent protein (GFP-HUVECs, Angio-Proteomie), and normal human lung fibroblasts (nHLFs, Lonza), and two media channels with endothelial cell monolayers. The channels were formed by bonding plasma-treated PDMS and glass coverslips (No. 1, Marienfeld), followed by polydopamine coating (5 mg/mL in pH 8.5 Tris HCL) for 45 min under UV light. The channels were then washed twice with distilled water and plasma-treated to increase hydrophilicity during seeding (100 W, 3 min). A thrombin solution (4 unit/ mL in EBM) containing GFP-HUVECs (19.6×10^6 cells/mL) and nHLFs (14×10^6 cells/mL) was mixed with a fibrinogen solution (6 mg/ mL in PBS) and immediately pipetted inside the gel channel. After the gelation, media channel was incubated with matrigel solution (300 µg/ mL in EBM) for 45 min and endothelial cells solution (4×10^6 cells/mL in EGM2-MV) were introduced in the media channel. Residual cells were removed after the attachment and the microfluidic device were daily refreshed with vascular endothelial growth factor supplemented EGM2-MV (20 ng/mL, Peprotech) inside the humidified incubator (5 % CO_2 at 37 °C). After vascularization for five days, patent lumens inside the VoC were perfused with EGM2-MV for an additional two days using a peristaltic pump (Takasago Fluidic Systems), the microfluidic device was fixed, permeabilized, and mounted with Vectashield (Vector Laboratories) before imaging. Over a period of five days, a continuous vessel network was formed within the ECM through vasculogenesis, which is the self-assembly of endothelial cells. This process was monitored by observing endothelial cell proliferation, elongation, and branching, which confirmed successful vascularization of the sample (supplementary figure S1).

For long-term live-cell monitoring experiments of tumor spheroid,

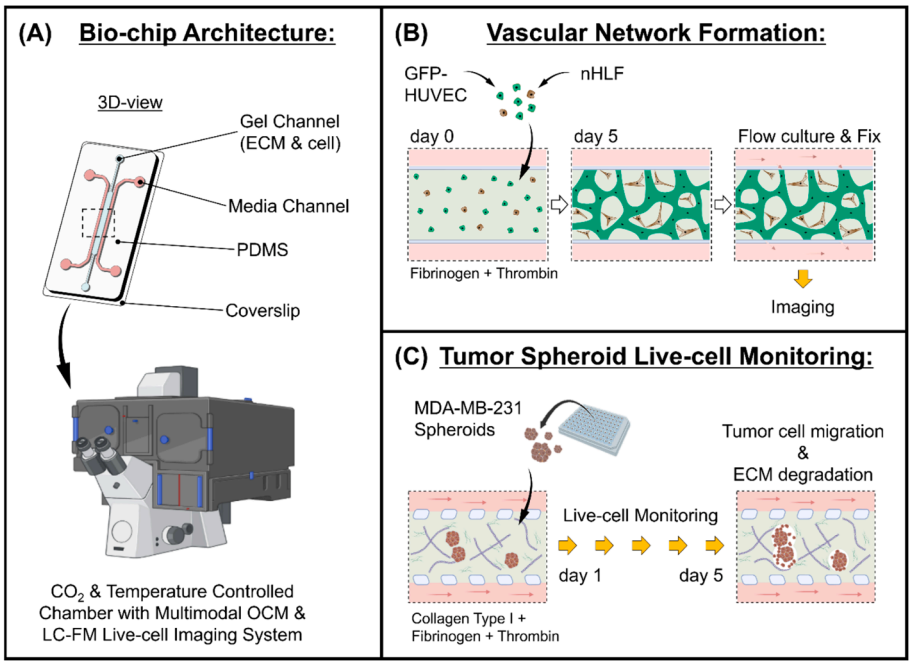

Fig. 3. Details of biochip sample architecture, vascular formation in VoC, and tumor spheroid sample preparation for long-term live-cell monitoring. (A) Overall architecture of the biochip and the environment controlled multimodal imaging system used for experiments. (B) Vascular network formation used for VoC samples. (C) Tumor spheroid formation in biochip used in long-term live-cell monitoring experiments.

the biochip containing the tumor spheroid was fabricated by injecting mixture of tumor spheroids, collagen type-I (Gibco, final 0.1 mg/ mL), fibrinogen (Sigma, final 2.5 mg/ mL), and thrombin (final 2 unit/ mL) into gel channel. The tumor spheroids were formed by co-culture of human breast cancer cells (MDA-MB-231, Korea Cell Line Bank) and human mammary fibroblasts (HPMF, Cell Biologics) for three days in PrimeSurface® 3D culture plate (S-bio). Both the cell types were stained with CellTracker Green (Invitrogen) before performing the co-culture for FM imaging. To supply the nutrients needed for cell growth, a warm (37 °C) media (RPMI1640, Gibco) was continuously injected into the biochip samples through the media channels using a syringe pump (Harvard Apparatus) and an inline heater (Fluidic Inline Heater, LCI, Inc.) for the entire experimental period (five days).

3. Results and discussion

3.1. *High-resolution FM imaging at desired locations within a 3D sample*

To reduce photobleaching and phototoxicity, which occur during fluorescence imaging of 3D samples, the fluorescence excitation time must be limited. With our proposed method, the three steps mentioned in Section 2.2, namely, determining an ROI, aiming to illuminate that ROI, and immediately performing high-resolution confocal FM imaging, were validated using 3D samples of tumor spheroids and vascular networks. Vascular networks and tumor spheroid formation on biochips are widely recognized as physiologically relevant in vitro models that well describe key aspects of the tissue microenvironment and disease pathophysiology. Moreover, evaluating 3D tissue models has emerged as a major challenge as the Food and Drug Administration (FDA) has recently permitted alternative approaches to *in vivo* models for regulatory purposes. Vascular network analysis is related to angiogenesis, an important process associated with tumor growth and metastasis. Tumor spheroid models are useful tools for studying tumor biology and drug discovery. High-resolution FM imaging was effectively performed on protrusions of a tumor spheroid and vascular branches using the proposed method.

3.1.1. *Tumor-associated protrusion*

Protrusions are known to correlate with the invasion potential of tumor spheroids. Increased protrusion fluctuations and long protrusions facilitate tumor invasion by breaching the basement-membrane barrier [39]. The LC-FM assisted by OCM successfully imaged these tumor-associated protrusions, highlighted within the ROI using red dashed circles in Fig. 4. Fig. 4 illustrates how OCM can be used to effectively locate a ROI in a 3D sample, which in this study is a protrusion of a tumor spheroid, and perform high-resolution fluorescence imaging directly on that ROI. As shown in the first step of Fig. 4, the sample was explored, and the ROI was determined. Fig. 4(A) displays a three-axes cross-sectional OCM image extracted from volumetric data acquired with 10 × objective. The intersection of the yellow dotted crosshairs in the three-axes cross-sectional OCM image indicates the location from which the image is extracted. The crosshairs can be moved as desired, and the corresponding cross-sectional images in all three-axes are updated in real time. This is useful for determining the ROI. Corresponding 10 × FM images and OCM volume-rendered images of the tumor spheroids are shown in Fig. 4(B) and (C). While the dotted pentagon highlighted in the OCM volumetric image in Fig. 4(C) shows a clear distribution of cells along the depth, this was difficult to observe in the 10 × FM image shown in Fig. 4(B). The ROI for the 60 × FM volume imaging was selected as the bottom structure, which appeared to be a round cellular structure with fiber-like protrusions. This is indicated by red dotted circles. In the second step, the goal was to focus the light on the 60 × FM imaging at the desired location within the ROI. First, the center of the ROI was positioned along the optical axis of the objective lens using a sample-movement stage. The conversion to 60 × OCM also involved the mechanical movement of the reference mirror and a change to the 60 × objective lens. The YZ image from the 60 × OCM appears line-like owing to the narrow depth-of-focus produced by the 60 × objective. Fig. 4(D1)–(D3) show the representative images when the objective is moved along the depth axis. Fig. 4(E1)–(E3) show the depth scan plots of the positions indicated by the solid yellow lines in (D1)–(D3). The inset in Fig. 4(E3) shows a histogram of 150 peak positions (objective depth position maintained) with a bin spacing of one image pixel and an X-axis interval at the middle depth of the channel. The

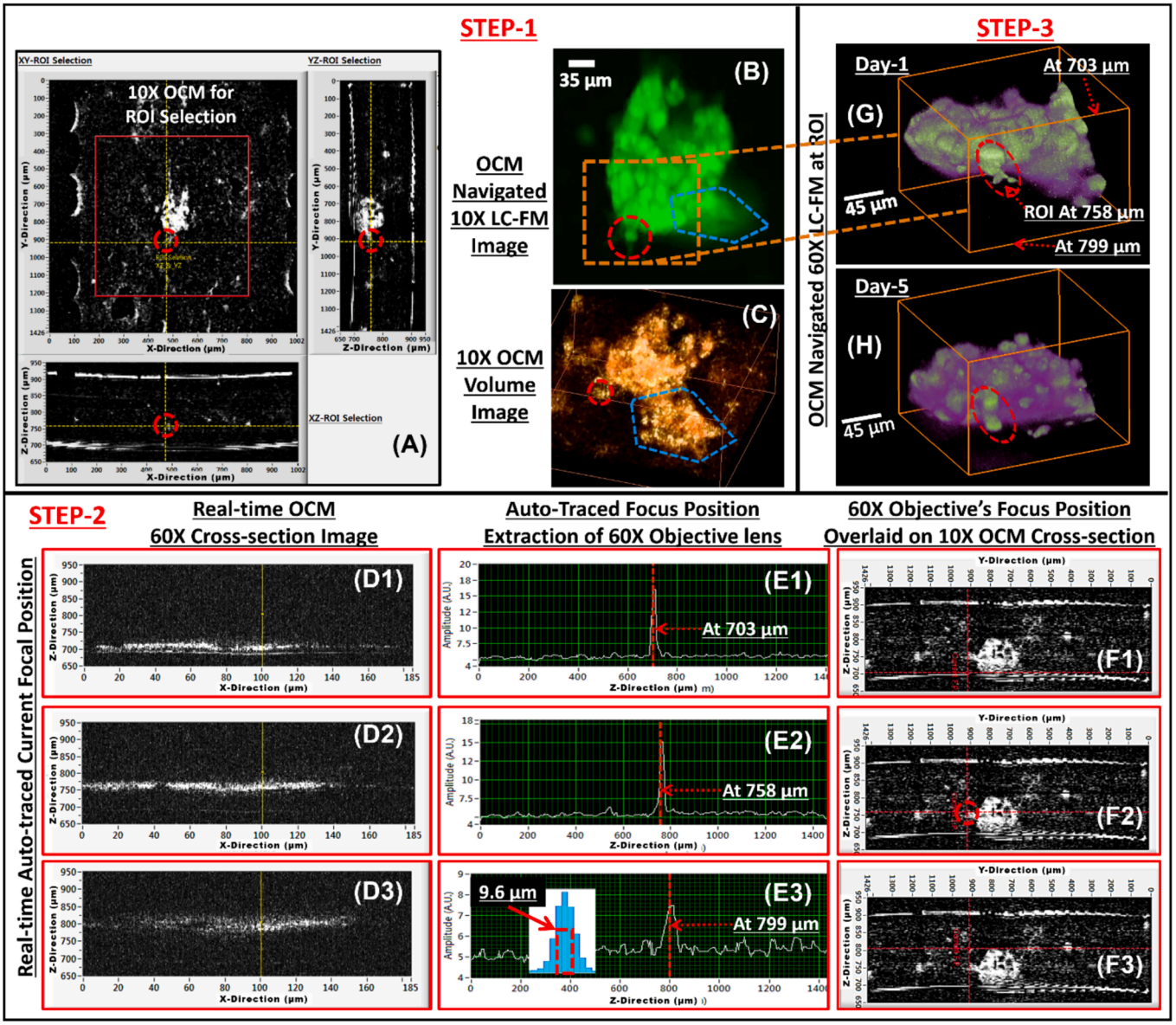

Fig. 4. 3D guidance employed by OCM for high-magnification LC–FM imaging in live-cell tumor spheroid monitoring. (A) shows the three-axes cross-sectional visualization extracted from the pre-stored 10 × OCM 3D image. (B) and (C) are the 10 × LC–FM and OCM volume rendered image. D1–D3 are real-time OCM 60 × cross-sectional images. The depth scan plots along the solid yellow line in (D1)–(D3) are (E1)–(E3). Inset in (E3) is the histogram plot of 150 peak positions of the depth scan plots. (F1)–(F3) are 10 × OCM cross-sectional images marked with auto-traced current 60 × focal position. (G) and (H) are the 60 × LC–FM image of targeted ROI on days 1 and 5 respectively. The red dotted circles and ellipse indicate the targeted ROI for LC–FM. (For interpretation of the references to colour in this figure legend, the reader is referred to the web version of this article.)

signal-to-noise ratio (SNR) of the peak signal, measured at this depth with a 60 × objective lens, was 1.5. The measured full width half maximum (FWHM) of the histogram was 9.6 µm, which corresponded to the accuracy of determining the depth of the focal position, and this accuracy is strongly correlated to the SNR. For SNR higher than 2, corresponding to Fig. 4(E1)-(E2), the accuracy is better than 3.2 µm, which corresponds to the pixel resolution of the OCM system. (F1)–(F3) are the auto-tracked current 60 × focal plane positions superimposed on the pre-saved 10 × OCM YZ cross-sectional image, with the current focal plane indicated by the red dotted horizontal line at the intersection. Additionally, at this stage, the depth boundaries of the ROI were recorded, and these values were used as the start and end points when scanning the z-axis for volumetric 60 × FM imaging. In the final step, the target ROI was directly imaged with 60 × FM. The z-axis sample stage is moved along the depth direction to obtain high-magnification FM volumetric images (G). The exact location of the ROI was 758 µm away from the surface of the biochip. The first and last focal plane boundaries of the ROI were at 703 and 799 µm from the biochip sample surface, and the overall thickness of the ROI was 96 µm. In Fig. 4, image (H) is a 60 × LC–FM volumetric image of the same target ROI taken on day 5 of the live-cell monitoring experiment. Overall structural changes that occurred during the monitoring experiment are shown in Fig. 4(G) and (H), with changes within the ROI highlighted by dashed elliptical circles.

In the observed OCM images and graphs presented in Fig. 4(D1-D3) and (E1-E3), a noticeable decrease in both SNR and FWHM is evident as the imaging depth increases. This phenomenon can be attributed to the inherent limitations associated with deep tissue imaging, particularly when using high NA objectives with a very narrow focus depth. High NA objectives are essential for achieving high-resolution imaging, as they enable the collection of a large portion of scattered light from the sample. However, when imaging deep into the tissue, high NA objectives face challenges related to optical scattering, aberrations, and dispersion.

Optical scattering occurs when light interacts with tissue structures, causing deviation and diffusion of light rays. As a result, the signal intensity decreases as imaging deep into the tissue, thus reducing SNR. Aberrations are caused by changes in refractive indices within tissue components such as cell membranes, organelles, and extracellular matrix. These varying refractive indices by complex microstructures lead to aberration effects that distort the wavefront and thus degrade lateral resolutions as light travels deeper into the tissue. Additionally, dispersion in tissue leads to axial PSF broadening in OCM, reducing axial resolvability. This dispersion phenomenon becomes more profound as light propagates through deeper tissue layers, resulting in decreased depth resolution. Consequently, the imaging depth achievable with high NA objectives is constrained, and the quality of images acquired from deeper tissue regions is compromised. To address these limitations, various strategies can be employed to improve deep tissue imaging performance in future studies. These may include software-controlled increasing laser power of OCM as imaging deeper into tissues to compensate the signal attenuation, adaptive optics to correct aberrations, and signal processing algorithms to reduce dispersion.

3.1.2. *Narrow tubular branches in the 3D vascular network*

During angiogenesis, blood vessel branching is an important morphogenetic process to grow complex vascular networks and related to angiogenic sprouting and tumor growth [40]. OCM imaging allows visualization of the complex vascular structures in 3D tissue models, as shown in Fig. 5. This feature enables a comprehensive study of the locations of small blood vessel branches and angiogenic sprouts within a sample, minimizing the labor-intensive process in implementing 3D

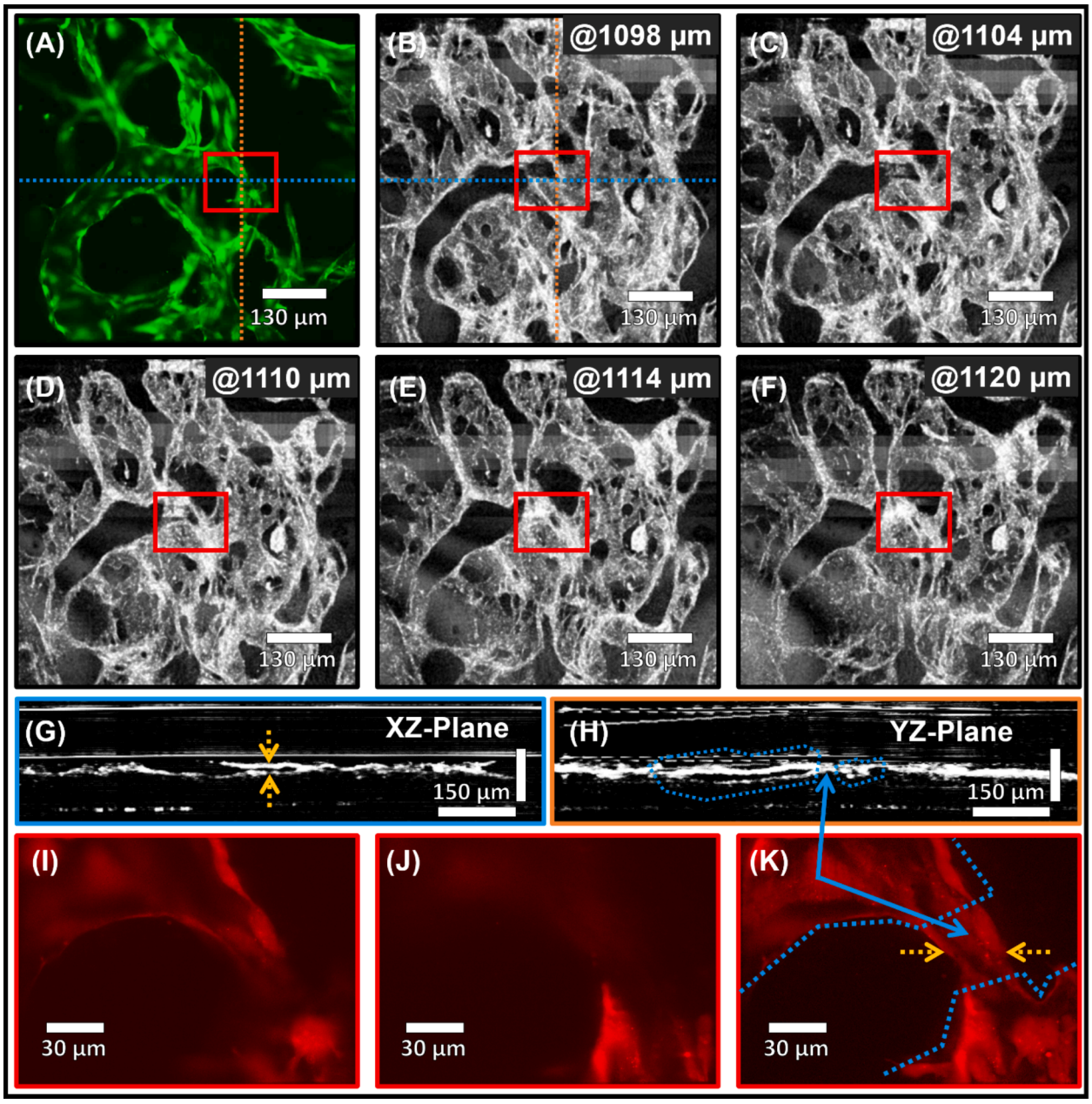

Fig. 5. Visualization of vascular branching along depth in VoC using OCM guided ROI selection for 60 × LC–FM imaging. (A) 10 × LC–FM vascular network image selected via OCM three-axes cross-sectional guidance. Images (B)–(F) are successive OCM *en face* images along the depth axis. (G) and (H) are the cross-sectional OCM images captured at the positions marked with the blue dotted and orange dotted cross-hairs in (A) and (B). The red solid box in (A)–(F) is the targeted ROI. (I)–(K) ROI of 60 × LC–FM images. (I) and (J) are the top and bottom planes of the ROI. Projection image (K) is obtained from (I) and (J). (For interpretation of the references to colour in this figure legend, the reader is referred to the web version of this article.)

tissue models. Fig. 5 (A) shows the vascular network image obtained with 10 × LC–FM of the VoC sample, which was selected using OCM's three-axes cross-sectional guidance. Images in Fig. 5(B)–(F) show successive OCM *en face* images to visualize the changes occurring in the vascular structures along the depth. The small vascular branching ROI selected for LC–FM 60 × imaging is highlighted within the red-box region in Fig. 5(A)–(F). The selected ROI shows clear branching of the vascular network, which is well-defined as shown in cross-sectional OCM images in Fig. 5(G), (H) and successive *en face* OCM along the depth. Image (G) is the OCM cross-sectional image (X-Z) corresponding to the position of the blue dashed line, and image (H) is the OCM cross-sectional image (Y-Z) corresponding to the position of the orange dashed line of the cross-hair in Fig. 5(A) and (B). In Fig. 5, images (I)–(K) are 60 × LC–FM images of the target ROI, and Fig. 5(I) and (J) are topmost and bottommost boundary sections of the vascular network branch, respectively. The two boundary depths were aimed directly using the proposed method. In Fig. 5, image (K) was obtained by summing images in Fig. 5 (I) and (J) in post-image processing. The vascular branch is 23 μm thick and 30 μm wide. The width of the vascular branch was measured using the LC–FM 60 × image indicated by the yellow dashed inward-pointed arrows in Fig. 5(K), while its thickness was measured using the OCM cross-sectional XZ image indicated by the yellow dashed inward-pointed arrows in Fig. 5(G). The vascular branching section of the ROI is indicated by solid blue arrows in the OCM –XZ and YZ cross-sectional in Fig. 5(G) and (H), and in the LC–FM projection image Fig. 5(K).

3.2. Observation of cell behaviors in long-term 3D cultures using FM–OCM complementary imaging

The 3D culture format of organoids and spheroids utilizes the ECM that better represents *in vivo* physiology and genetic diversity than traditional two-dimensional cell lines because the ECM constitutes the primary acellular microenvironment of cells in nearly all tissues and organs. The ECM not only provides mechanical support but also mediates numerous biochemical interactions to guide cell survival, proliferation, differentiation, and migration. Therefore, much research is being conducted on the effects of ECM-based biomaterials on cellular behavior. To evaluate the advantages of the FM–OCM complementary imaging technique, we applied the proposed method to real cases of cell proliferation and migration of tumor spheroids mixed with ECM in long-term 3D culture. Reliably imaging the shape and changes in the 3D structure of the ECM using OCM is helpful for observing cell behavior within microenvironments such as the ECM.

3.2.1. Proliferation and migration of tumor cells in the ECM

All the images shown in Fig. 6 were captured using a 10 × objective lens. Fig. 6(A) and (B) show the reconstructed volumetric images of a tumor spheroid taken on days-1 and 5, and the corresponding FM images of the same position are shown in Fig. 6(E) and (F). Fig. 6(C) shows an overlay of Fig. 6(A) and (B). Similarly, Fig. 6(G) shows an overlay of Fig. 6(E) and (F). In the overlay image of Fig. 6(C), the day-1 OCM volume of the spheroids is shown in grayscale, while day-5 is colored

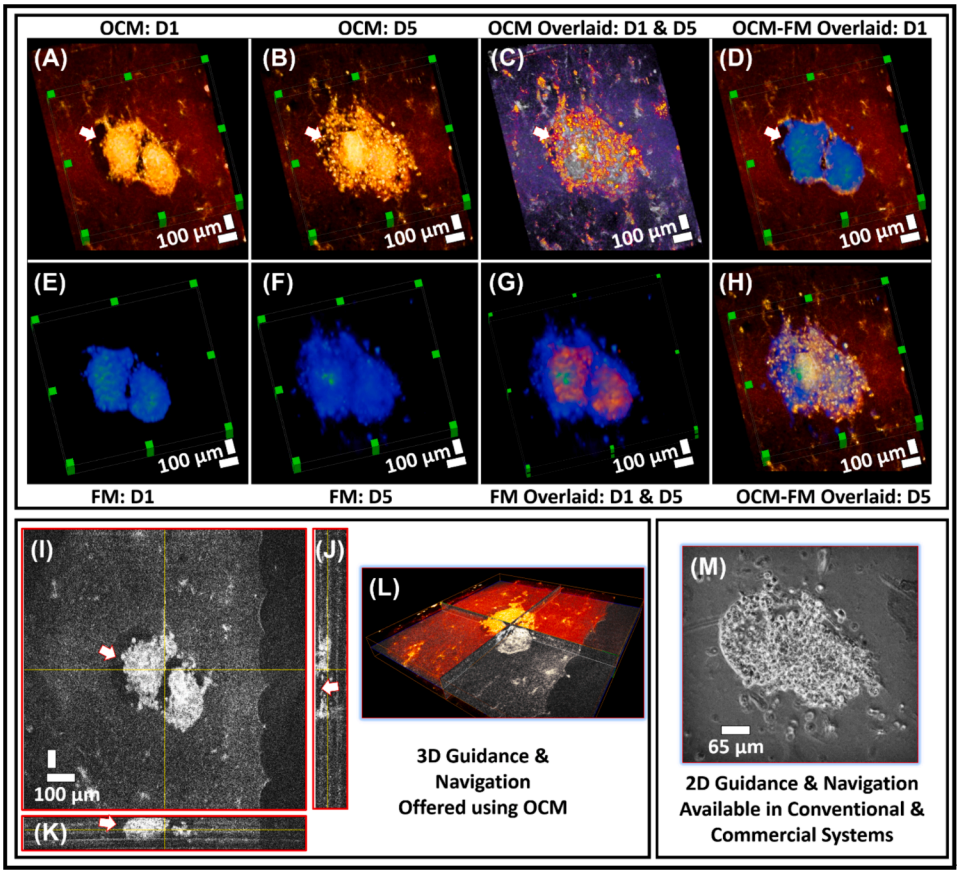

Fig. 6. Complementary utilization of OCM and LC–FM imaging in tumor spheroid live-cell monitoring and advantages of 3D ROI selection and navigation using OCM over conventional phase microscopy for navigation and guidance for FM imaging. (A)-(B) and (E)-(F) are reconstructed 10 × OCM volumetric images, and 10 × LC–FM images of tumor spheroids on days 1 and 5, respectively. (C) is the overlay of (A) and (B). (G) is the overlay of (E) and (F). (D) and (H) are overlays of (A) and (E), and (B) and (F) respectively. (I)–(L) are the *en face*, vertical cross-sectional, horizontal cross-sectional, and 3D reconstructed OCM volumetric images with orthogonally sliced intersection of (A). (M) is the conventional guidance for FM imaging using phase contrast microscopy topological image of tumor spheroid on day-5. The white arrows in (A)–(D) and (I)–(K) are the hollow voids surrounding and in-between two spheroids, which are not visible in the LC–FM or in-phase contrast microscopy images.

orange to blue, with orange representing the highest intensity. Similarly, in Fig. 6(G), the day-1 FM image is in orange and day-5 is blue. In addition, Fig. 6(D) and (H) show the overlays of the OCM and LC–FM images captured on days-1 and 5, respectively. As shown in Fig. 6(C) and (G), the two spheroids grew and clumped into one large spheroid over time. A time-lapse of this is shown as a video in Supplementary video file S2. However, in the OCM volumetric image shown in Fig. 6(C), it is clear that the border cells of the spheroid move outward rather than simply remaining stationary and proliferating. This was not noticeable when using the FM, as shown in Fig. 6(G). This may be because the fluorescence signal weakens over time and the sensitivity of OCM is higher than that of FM. Additionally, areas devoid of the ECM gel (indicated by white arrows in Fig. 6(A)–(D) and (I)–(K)) were visible around and between the spheroids in the OCM images. However, this is not visible in FM or is difficult to distinguish even in phase-contrast microscopy, as shown in Fig. 6(M). This is a tumor invasion in which tumor cells appear to migrate outward after ECM degradation, demonstrating the potential of using OCM imaging to understand the tumor cell migration mechanisms associated with the ECM. Commonly used and widely adopted phase-contrast microscopy images provide only a two-dimensional (2D) topological view of the spheroid, as shown in Fig. 6 (M), and cannot fully realize the complex volumetric structure formation of the spheroid. On the other hand, OCM offers a real-time *en face* image of Fig. 6(I) and cross-sectional images of Fig. 6(J) and (K), which are useful for better understanding spheroid and ECM structures. Additionally, the 3D volumetric image of Fig. 6(L) of the sample can be visualized for intuitive understanding. Therefore, OCM volume imaging enables the analysis of tumor cell invasion and ECM remodeling, which includes ECM generation and degradation in the 3D volume.

3.2.2. *Migration of tumor cells along collagen fibers*

Tumor spheroid samples were explored using 10 × OCM imaging, and single tail-shaped protrusions emanating from the lower region of the spheroid were designated as ROI and observed during five days of culture, as shown in Fig. 7. Fig. 7 (A) and (B) show images in which a 60 × magnification FM image (green hue) of the ROI is superimposed on a

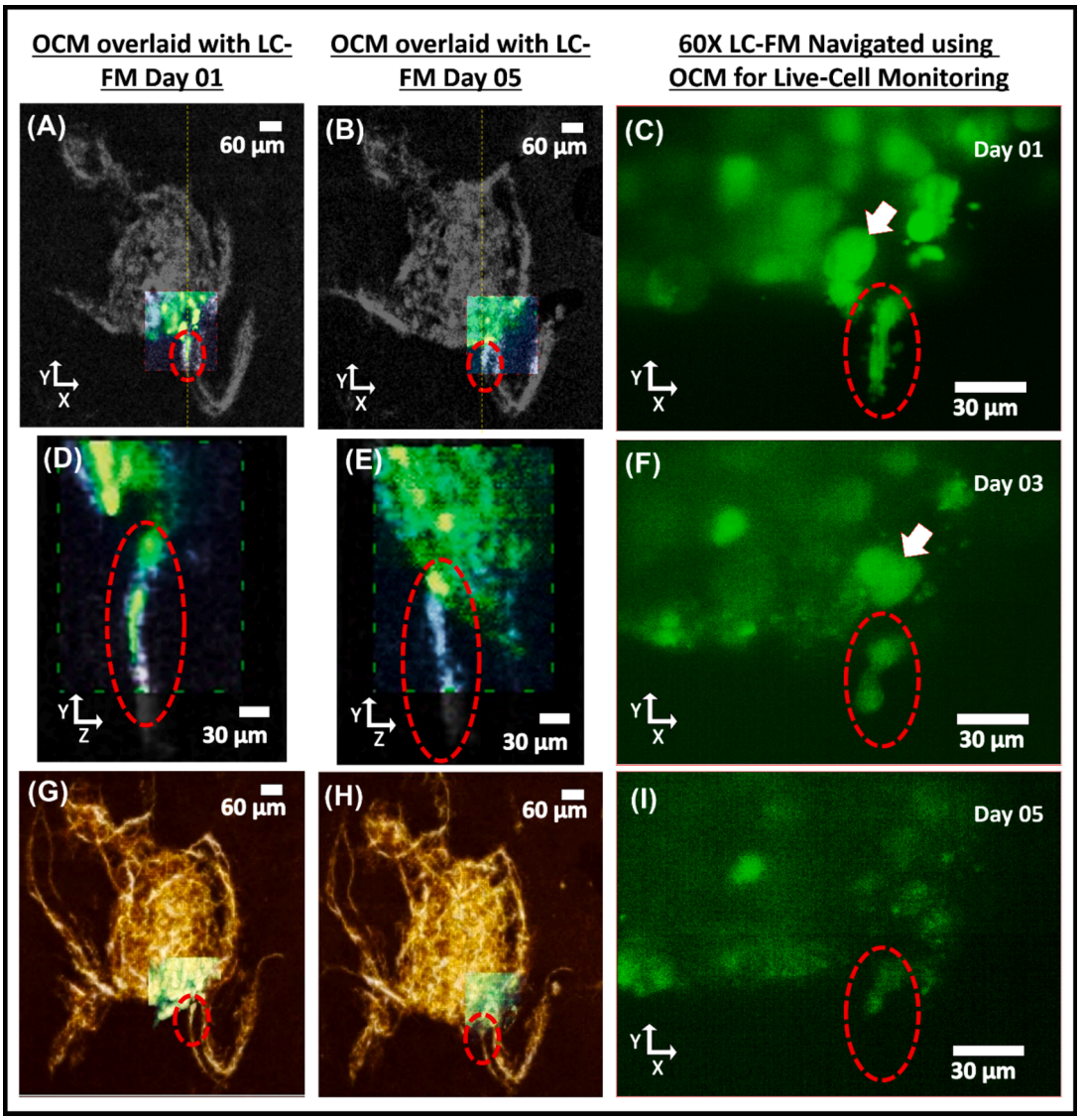

Fig. 7. OCM-assisted FM in live-cell monitoring. (A), (B) cross-sectional images; (D), (E), (G), and (H) are 10 × OCM images overlaid with 60 × LC–FM image of a tumor spheroid. (C), (F), and (I) are the 60 × LC–FM live-cell monitoring images obtained on days 1, 3, and 5 using the OCM-based 3D navigation method. The real-time OCM cross-sectional images (D) and (E) are obtained at the position indicated with the yellow dashed line in the real-time *en face* images (A) and (B), respectively. The structures indicated within red dotted ellipse and with white arrows in all the images highlight the changes that occurred during the monitoring period. The LC–FM images are presented in the green hue, and the images in grayscale represent the cross-sectional and *en face* OCM images, while those in orange hue are the 3D OCM images. (For interpretation of the references to colour in this figure legend, the reader is referred to the web version of this article.)

10 × magnification OCM image (gray hue). Fig. 7(A) was acquired on the first day, and Fig. 7(B) on the fifth day. Fig. 7(D) shows a cross-sectional (x-z) image of the ROI at the location indicated by the yellow dotted line in Fig. 7(A), and Fig. 7(E) shows a cross-sectional (x-z) image of Fig. 7(B). The 3D volume-rendered images are displayed in orange to provide a comprehensive visualization of the tissue morphology, as shown in Fig. 7(G) and (H), corresponding to days 1 and 5 of the culture, respectively. A 60 × FM image of the ROI was added to the 3D volume-rendered image. And Fig. 7(C), (F), and (I) correspond to the 60 × FM images of the ROI acquired on days 1, 3, and 5 of culture, respectively. The tail-shaped protrusion within the ROI gradually shrank over time, as indicated by the dashed red circles in Fig. 7. As can be seen in the *en face* (x-y) image in Fig. 7(A-B) and the cross-sectional (x-z) image in Fig. 7(D-E), OCM can observe protruding collagen fibers in three-dimensions. Through the OCM–FM complementary imaging, it was possible to confirm that the tumor cells migrated along the fiber bundle. Because ECM fibers are continuously remodeled during tumor growth and metastasis, a label-free imaging tool is necessary, and combining OCM with LC–FM could be a solution. Additionally, the tumor volume can be accurately measured using OCM volumetric imaging. The measured total volumes of the tumor spheroids were 3.45×10^6 μm^3 and 5.32×10^6 μm^3 on days 1 and 5, respectively, resulting in a total increase of 1.87×10^6 μm^3 in the volume. On average, the measured tumor volume using 3D volume imaging identified tumor invasion by volume increased by 1.5 to 2×10^6 μm^3. Exact measurement of tumor volume in three-dimensions is crucial to sensitively determine the effectiveness of anticancer drugs. Therefore, OCM combined with LC–FM is a useful tool for comprehensive analysis of tumor growth and metastasis correlated with ECM and drug testing.

4. Conclusions

We presented a multimode and multiscale FM–OCM amalgamated imaging system for co-registration acquisition of LC–FM and OCM images; this system can be used with different objectives for low and high imaging magnifications. Based on this imaging system, we proposed a method for high-resolution 3D fluorescence imaging directly at the desired location. This method helped to reduce the risk of phototoxicity and photobleaching in thick samples by selectively using fluorescent signals from specific areas of interest within a 3D sample. It also reduced the time and effort required for ROI selection and navigation in high-resolution LC–FM imaging. We demonstrated the use of complementary information obtained from OCM to identify morphologically interesting regions of cells and tissues. This helps to continuously observe morphological changes without consuming the fluorescent signal resources for long-term FM analysis of living cells. To evaluate the performance and test the applicability of the proposed system and method, 3D live-cell models such as tumor spheroids and self-assembled vascular network were cultured on a biochip for five days and imaged. Specifically, we precisely searched for protrusions outside the tumor spheroids and narrow tubular branches of the 3D vascular network and instantaneously performed high-resolution FM imaging. We also demonstrated the advantages of the OCM–FM complementary imaging method by analyzing cell proliferation and migration of mixed tumor spheroids in the ECM and microenvironment in long-term 3D cultures. Nevertheless, there are the limitations of our proposed method compared to alternative multimodal imaging techniques. For instance, 3D holography integrated fluorescence microscopy can enable rapid 3D imaging of samples, calculate the refractive index changes within the sample structures [41]. However, these applications are limited to transparent or thin sample. Another multimodal imaging approach is the use of fluorescence microscopy in combination with multiphoton microscopy [42]. The use of multiphoton imaging aids in imaging deep into tissues, as long-wavelength excitation sources enable imaging at depths beyond 1 mm [43]. However, the long exposure duration of high-intensity multiphoton lasers can cause phototoxicity to the sample structures. Furthermore, our proposed method addresses the need for depth-resolved fluorescence imaging in thick tissue samples, but it may not be fully utilized due to limitations associated with optical scattering, aberration and dispersion, particularly in deep-tissue imaging applications. This has been further discussed in detail in section 3.1.1. Future studies will be focused on the addition of flow and photothermal detection functions to the OCM and expansion of confocal FM into a multicolor imaging system for investigation of the flow and photothermal effects of nanoparticles in engineered microsystems.

Funding

This study was supported by the Korea Basic Science Institute [Grant number: D300300].

CRediT authorship contribution statement

Naresh Kumar Ravichandran: Investigation, Software, Visualization, Writing – original draft. **HyeMi Kim:** Investigation, Resources, Visualization, Writing – original draft. **Joonha Park:** Investigation, Resources, Visualization, Writing – original draft. **Hwan Hur:** Writing – review & editing. **Jinsung Kim:** Writing – review & editing. **Ji Yong Bae:** Writing – review & editing. **Sangwon Hyun:** Writing – review & editing. **I. Jong Kim:** Writing – review & editing. **Dong Uk Kim:** Writing – review & editing. **Sang-Chul Lee:** Writing – review & editing. **Ki Soo Chang:** Writing – review & editing. **Inbarasan Muniraj:** Writing – review & editing. **Jessie S. Jeon:** Supervision, Writing – review & editing. **Ki-Hwan Nam:** Supervision, Writing – review & editing. **Kye-Sung Lee:** Conceptualization, Methodology, Software, Supervision, Writing – review & editing.

Declaration of competing interest

The authors declare that they have no known competing financial interests or personal relationships that could have appeared to influence the work reported in this paper.

Data availability

Data will be made available on request.

Appendix A. Supplementary data

Supplementary data to this article can be found online at https://doi.org/10.1016/j.optlastec.2024.111351.

References

[1] A. Ettinger, T. Wittmann, Fluorescence Live Cell Imaging vol. 123 (2014), https://doi.org/10.1016/B978-0-12-420138-5.00005-7.
[2] T.A. Mekuria, M.Z. Kinde, Basic principles and applications of live cell microscopy techniques: a review, World's Vet. J. 12 (2022) 339–346, https://doi.org/10.54203/SCIL.2022.WVJ43.
[3] J.C. Waters, Live-Cell Fluorescence Imaging vol. 114 (2013), https://doi.org/10.1016/B978-0-12-407761-4.00006-3.
[4] V.P. Nguyen, W. Fan, T. Zhu, W. Qian, Y. Li, B. Liu, et al., Long-term, noninvasive in vivo tracking of progenitor cells using multimodality photoacoustic, optical coherence tomography, and fluorescence imaging, ACS Nano 15 (2021) 13289–13306, https://doi.org/10.1021/acsnano.1c03035.
[5] L. Hof, T. Moreth, M. Koch, T. Liebisch, M. Kurtz, J. Tarnick, et al., Long-term live imaging and multiscale analysis identify heterogeneity and core principles of epithelial organoid morphogenesis, BMC Biol.. 19 (2021) 1–22, https://doi.org/10.1186/s12915-021-00958-w.
[6] L. Zhang, Y. Ding, X. Chen, D. Xiang, F. Shi, Y. Chen, et al., In vivo fluorescence molecular imaging of the vascular endothelial growth factor in rats with early diabetic retinopathy, Biomed. Opt. Express 12 (2021) 7185, https://doi.org/10.1364/boe.439446.
[7] G. Sancataldo, L. Silvestri, A.L. Allegra Mascaro, L. Sacconi, F.S. Pavone, Advanced fluorescence microscopy for in vivo imaging of neuronal activity, Optica 6 (2019) 758, https://doi.org/10.1364/optica.6.000758.

[8] J. Icha, M. Weber, J.C. Waters, C. Norden, Phototoxicity in live fluorescence microscopy, and how to avoid it, Bioessays 39 (2017) 1–15, https://doi.org/10.1002/bies.201700003.
[9] A.P. Demchenko, Photobleaching of organic fluorophores: quantitative characterization, mechanisms, protection, Methods Appl. Fluoresc. 8 (2020) 022001, https://doi.org/10.1088/2050-6120/ab7365.
[10] H. Gundlach, C.Z. Jena, Multiple Fluorescence Microscopy and Optoelectronic Imagin g - Possibilities and Limits 3197, 214–216.
[11] A. Orth, R.N. Ghosh, E.R. Wilson, T. Doughney, H. Brown, P. Reineck, et al., Super-multiplexed fluorescence microscopy via photostability contrast, Biomed. Opt. Express 9 (2018) 2943, https://doi.org/10.1364/boe.9.002943.
[12] R.P. Baker, M.J. Taormina, M. Jemielita, R. Parthasarathy, A combined light sheet fluorescence and differential interference contrast microscope for live imaging of multicellular specimens, J. Microsc. 258 (2015) 105–112, https://doi.org/10.1111/jmi.12220.
[13] B.G. Hosu, W. Hill, A.D. Samuel, H.C. Berg, Synchronized strobed phase contrast and fluorescence microscopy: the interlaced standard reimagined, Opt. Express 31 (2023) 5167, https://doi.org/10.1364/oe.474045.
[14] N.B. Vicente, J.E. Diaz Zamboni, J.F. Adur, E.V. Paravani, V.H. Casco, Photobleaching correction in fluorescence microscopy images, J. Phys. Conf. Ser. (2007) 90, https://doi.org/10.1088/1742-6596/90/1/012068.
[15] S.N. Bhatia, D.E. Ingber, Microfluidic organs-on-chips, Nat. Biotechnol. 32 (2014) 760–772, https://doi.org/10.1038/nbt.2989.
[16] D. Huh, G.A. Hamilton, D.E. Ingber, From 3D cell culture to organs-on-chips, Trends Cell Biol. 21 (2011) 745–754, https://doi.org/10.1016/j.tcb.2011.09.005.
[17] C.M. Leung, P. de Haan, K. Ronaldson-Bouchard, G.A. Kim, J. Ko, H.S. Rho, et al., A guide to the organ-on-a-chip, Nat. Rev. Methods Prim. (2022) 2, https://doi.org/10.1038/s43586-022-00118-6.
[18] G.S. Kronemberger, F.A. Carneiro, D.F. Rezende, L.S. Baptista, Spheroids and organoids as humanized 3D scaffold-free engineered tissues for SARS-CoV-2 viral infection and drug screening, Artif. Organs 45 (2021) 548–558, https://doi.org/10.1111/aor.13880.
[19] R.Z. Lin, H.Y. Chang, Recent advances in three-dimensional multicellular spheroid culture for biomedical research, Biotechnol. J. 3 (2008) 1172–1184, https://doi.org/10.1002/biot.200700228.
[20] D.A. Gil, D.A. Deming, M.C. Skala, Volumetric growth tracking of patient-derived cancer organoids using optical coherence tomography, Biomed. Opt. Express 12 (2021) 3789, https://doi.org/10.1364/boe.428197.
[21] W. Liu, G.A.R. Kim, S. Takayama, S. Jia, Fourier light-field imaging of human organoids with a hybrid point-spread function, Biosens. Bioelectron. 208 (2022) 114201, https://doi.org/10.1016/j.bios.2022.114201.
[22] S. Pant, C. Li, Z. Gong, N. Chen, Line-scan focal modulation microscopy, J. Biomed. Opt. 22 (2017) 1, https://doi.org/10.1117/1.jbo.22.5.050502.
[23] S. Hayashi, Y. Okada, Ultrafast superresolution fluorescence imaging with spinning disk confocal microscope optics, Mol. Biol. Cell 26 (2015) 1743–1751, https://doi.org/10.1091/mbc.E14-08-1287.
[24] R. Turcotte, C.C. Schmidt, M.J. Booth, N.J. Emptage, Volumetric two-photon fluorescence imaging of live neurons using a multimode optical fiber, Opt. Lett. 45 (2020) 6599, https://doi.org/10.1364/ol.409464.
[25] J.-Y. Yu, M. Ouyang, C.-L. Guo, C.-H. Kuo, R. Zadoyan, D.B. Holland, et al., Wide-field optical sectioning for live-tissue imaging by plane-projection multiphoton microscopy, J. Biomed. Opt. 16 (2011) 1, https://doi.org/10.1117/1.3647570.
[26] G. de Medeiros, R. Ortiz, P. Strnad, A. Boni, F. Moos, N. Repina, et al., Multiscale light-sheet organoid imaging framework, Nat. Commun. 13 (2022) 1–14, https://doi.org/10.1038/s41467-022-32465-z.
[27] B. Isherwood, P. Timpson, E.J. Mcghee, K.I. Anderson, M. Canel, A. Serrels, et al., Live cell in vitro and in vivo imaging applications: Accelerating drug discovery, Pharmaceutics 3 (2011) 141–170, https://doi.org/10.3390/pharmaceutics3020141.
[28] A.F. Fercher, W. Drexler, C.K.L. Hitzenberger, Optical coherence tomography - principles and applications, vol. 66, 2003.
[29] J. Kim, W. Brown, J.R. Maher, H. Levinson, A. Wax, Functional optical coherence tomography: Principles and progress, Phys. Med. Biol. 60 (2015) R211–R237, https://doi.org/10.1088/0031-9155/60/10/R211.
[30] Y. Ming, S. Hao, F. Wang, Y.R. Lewis-Israeli, B.D. Volmert, Z. Xu, et al., Longitudinal morphological and functional characterization of human heart organoids using optical coherence tomography, Biosens. Bioelectron. 207 (2022) 114136, https://doi.org/10.1016/j.bios.2022.114136.
[31] W. Shi, L. Reid, Y. Huang, C.G. Uhl, R. He, C. Zhou, et al., Bi-layer blood vessel mimicking microfluidic platform for antitumor drug screening based on co-culturing 3D tumor spheroids and endothelial layers, Biomicrofluidics (2019) 13, https://doi.org/10.1063/1.5108681.
[32] Y.B. Arik, W. Buijsman, J. Loessberg-Zahl, C. Cuartas-Vélez, C. Veenstra, S. Logtenberg, et al., Microfluidic organ-on-a-chip model of the outer blood-retinal barrier with clinically relevant read-outs for tissue permeability and vascular structure, Lab Chip 21 (2021) 272–283, https://doi.org/10.1039/d0lc00639d.
[33] S. Lee, M.W. Lee, H.S. Cho, J.W. Song, H.S. Nam, D.J. Oh, et al., Fully integrated high-speed intravascular optical coherence tomography/near-infrared fluorescence structural/molecular imaging in vivo using a clinically available near-infrared fluorescence-emitting indocyanine green to detect inflamed lipid-rich atherom, Circ. Cardiovasc. Interv. 7 (2014) 560–569, https://doi.org/10.1161/CIRCINTERVENTIONS.114.001498.
[34] M. Andreana, R. Sentosa, M.T. Erkkilä, W. Drexler, A. Unterhuber, Depth resolved label-free multimodal optical imaging platform to study morpho-molecular composition of tissue, Photochem. Photobiol. Sci. 18 (2019) 997–1008, https://doi.org/10.1039/c8 pp00410b.
[35] J. Scholler, K. Groux, O. Goureau, J.A. Sahel, M. Fink, S. Reichman, et al., Dynamic full-field optical coherence tomography: 3D live-imaging of retinal organoids, Light Sci. Appl. (2020) 9, https://doi.org/10.1038/s41377-020-00375-8.
[36] S. Shrestha, M.J. Serafino, J. Rico-Jimenez, J. Park, X. Chen, S. Zhaorigetu, et al., Multimodal optical coherence tomography and fluorescence lifetime imaging with interleaved excitation sources for simultaneous endogenous and exogenous fluorescence, Biomed. Opt. Express 7 (2016) 3184, https://doi.org/10.1364/boe.7.003184.
[37] American National Standard for the Safe Use of Lasers. ANSI Stand Z136 1 2014. doi: 10.7326/0003-4819-82-1-132_2.
[38] J. Park, S. Kim, J. Hong, J.S. Jeon, Enabling perfusion through multicellular tumor spheroids promoting lumenization in a vascularized cancer model, Lab Chip 22 (2022) 4335–4348, https://doi.org/10.1039/d2lc00597b.
[39] D. Caballero, V. Brancato, A.C. Lima, C.M. Abreu, N.M. Neves, V.M. Correlo, et al., Tumor-associated protrusion fluctuations as a signature of cancer invasiveness, Adv. Biol. (2021) 5, https://doi.org/10.1002/adbi.202101019.
[40] A.C. Dudley, A.W. Griffioen, Pathological angiogenesis: mechanisms and therapeutic strategies, Angiogenesis 26 (2023) 313–347, https://doi.org/10.1007/s10456-023-09876-7.
[41] M. Kumar, X. Quan, Y. Awatsuji, C. Cheng, M. Hasebe, Y. Tamada, et al., Common-path multimodal three-dimensional fluorescence and phase imaging system, J. Biomed. Opt. 25 (2020) 1, https://doi.org/10.1117/1.jbo.25.3.032010.
[42] W.R. Zipfel, R.M. Williams, R. Christiet, A.Y. Nikitin, B.T. Hyman, W.W. Webb, Live tissue intrinsic emission microscopy using multiphoton-excited native fluorescence and second harmonic generation, PNAS 100 (2003) 7075–7080, https://doi.org/10.1073/pnas.0832308100.
[43] D.R. Miller, J.W. Jarrett, A.M. Hassan, A.K. Dunn, Deep tissue imaging with multiphoton fluorescence microscopy, Curr. Opin. Biomed. Eng. 4 (2017) 32–39, https://doi.org/10.1016/j.cobme.2017.09.004.